sustainability

Article

Utilizing the Taguchi Method to Optimize Rotor Blade Geometry for Improved Power Output in Ducted Micro Horizontal-Axis Wind Turbines

Kwan Ouyang , Tzeng-Yuan Chen * and Jun-Jie You

Department of Aerospace Engineering, Tamkang University, No.151, Yingzhuan Rd., Tamsui Dist., New Taipei City 251301, Taiwan; kouyang@mail.tku.edu.tw (K.O.); jun06069022@gmail.com (J.-J.Y.)
* Correspondence: tychen@mail.tku.edu.tw; Tel.: +886-2-26215656 (ext. 2779)

Abstract: This numerical study utilized the Taguchi method to systematically optimize the blade geometry of a ducted micro horizontal-axis wind turbine (HAWT) for moving vehicles to enhance the output power coefficient. Three geometric parameters of the rotor, namely, the number of blades, rotor solidity, and blade pitch angle, were investigated. The optimum parameter design includes eight blades, rotor solidity of 60%, and a pitch angle of 30°, where the blade pitch angle had the most significant effect on the rotor performance. This result confirms that high rotor solidity is more suitable for micro HAWT. The $C_{P,max}$ value achieved with the optimum geometry was 0.432, which was 39.4% higher than that achieved with the worst blade geometry. The aerodynamic characteristics of this wind turbine were also investigated. Compared with the worst blade geometry, the rotor with the optimum blade geometry drew more airflow into the duct and exhibited a higher $C_{P,max}$ due to a greater pressure difference between the windward and leeward sides of the blades. The optimum blade geometry achieved a $C_{T,max}$ of 0.43, which was 38.7% higher than the worst blade geometry. The investigated untwisted blades exhibited low torque near their tips; therefore, the use of twisted blades is recommended for further increasing the torque generated at the blade tip and thus the turbine's output power. This study facilitates insight into blade geometry effects on rotor performance and helps improve wind energy efficiency, contributing to sustainable development goals (SDGs) like SDG 7 (affordable and clean energy).

Keywords: micro horizontal-axis wind turbine; numerical simulation; optimization; rotor blade geometry; Taguchi method

check for updates

Citation: Ouyang, K.; Chen, T.-Y.; You, J.-J. Utilizing the Taguchi Method to Optimize Rotor Blade Geometry for Improved Power Output in Ducted Micro Horizontal-Axis Wind Turbines. *Sustainability* **2024**, *16*, 4692. https://doi.org/10.3390/su16114692

Academic Editors: Byungik Chang and Firoz Alam

Received: 4 April 2024
Revised: 29 May 2024
Accepted: 29 May 2024
Published: 31 May 2024

1. Introduction

To achieve sustainability and mitigate the effects of global warming, countries worldwide are beginning to use green energy as a substitute for traditional fossil fuel energy. Wind energy is a crucial source of green energy, because this energy is renewable and inexhaustible. Horizontal-axis wind turbines (HAWTs) are frequently used to capture wind energy and convert it into electricity. Numerous scholars have attempted to optimize wind turbine design to improve the efficiency with which this conversion is achieved. The performance of wind turbines can be improved through various methods, such as utilizing efficient airfoils, optimizing blade design, incorporating ducted wind turbines, and so on [1–3]. Using efficient airfoils and blade design optimization is a conventional technique for improving wind turbine efficiency, because the blades are the most crucial parts of a wind turbine. The aerodynamics of airfoils and blades, the rotor solidity and number of blades, and the angle of attack and pitch angle of blades are crucial in wind turbine performance. Much of the previous literature often analyzed the effects of parameters on rotor performance using one-factor-at-a-time investigations. However, this approach may introduce bias, as conclusions are drawn under specific experimental conditions, resulting in varying conclusions drawn under different experimental conditions. The present study used the Taguchi method to systematically optimize the rotor blade geometry, including the rotor solidity, number of blades, and blade pitch angle, of a ducted micro HAWT to improve its rotor performance. In addition, the airflow aerodynamic characteristics were investigated.

To obtain a better rotor performance, the airfoil of a turbine blade with a high lift-to-drag ratio (LDR) should be chosen. Chaudhry and Prakash [4] proposed six novel airfoils for the design of micro horizontal-axis wind turbines operating at low wind speeds. It was seen that the aerodynamic performance of NAF-Series airfoils was better than SG6043 and NACA4415 airfoils at a low Reynolds number, and NAF 4923 airfoil was the best candidate airfoil among others. Yossri et al. [5] numerically evaluated the aerodynamic performance of NACA0012, NACA4412, NACA0015, and NACA4415 airfoils with three rotor diameter sizes. The findings showed that the NACA 4412 airfoil yields the highest LDR of 26. The study conducted by Mostafa et al. [6] revealed that the SG6043 wind turbine blade has better aerodynamic performance, producing 2.5% more power than the NACA4412 blade under the same operating conditions. Suresh et al. [7] evaluated the aerodynamic performance of ten airfoils to examine the suitability of low-Reynolds-number airfoils for the design of a small-scale wind turbine at low wind conditions. The result revealed that the SG6043 airfoil had a maximum LDR of 56.40 at an eight-degree angle of attack. However, among these airfoils, the SD7080 airfoil was selected for the design of a wind turbine blade that can operate at low wind speed conditions. Abdelghany et al. [8] added a winglet at the blade tip to improve the aerodynamic characteristics of wind turbines. The results illustrate that the lift-to-drag ratio coefficient and power coefficient increase related to the blade without winglet by about 11.6% and 6.9%, respectively, at optimum winglet height lengths per blade radius of 0.042. Roy et al. [9] investigated the rotor performance and observed the flow characteristics around the NACA 4415 airfoils with protrusions in the leading edge on a horizontal-axis wind turbine. The results indicated that the best flow-controlling measures were achieved by using the spherical leading-edge protrusion (SLEP) model. The HAWT with SLEP exhibited an 8.2% greater power coefficient than that without leading-edge protrusion.

In the studies of blade design optimization, Duquette and Visser [10] numerically examined the effect of rotor solidity and the number of blades on the aerodynamic performance of a small HAWT. Their results indicated that under fixed rotor solidity, an increase in the number of blades leads to an increase in the maximum power coefficient of the rotor. Moreover, they found that an increase in rotor solidity from 5–7% to 15–25% causes an increase in $C_{P,max}$ and a reduction in the tip speed ratio (TSR). The TSR corresponding to $C_{P,max}$ varies considerably and marginally with a change in rotor solidity and the number of blades, respectively. Duquette et al. [11] experimentally evaluated the effects of rotor solidity and the number of blades on rotor performance. Their results indicated that C_P increased when the rotor solidity was increased from 7% to 27%; however, an increase in the number of blades did not result in a notable increase in C_P. For the optimum design of the three-blade rotor, an increase in solidity resulted in an increase in $C_{P,max}$ but a decrease in the TSR. At a fixed solidity of 10%, the aerodynamic efficiency and power sharply decreased when the number of blades was increased to 12. Leung et al. [12] numerically evaluated the performance of micro wind turbines with different design parameters. Their results indicated that high-solidity wind rotors outperformed low-solidity ones. The micro wind turbine with rotor solidity of more than 50% outperformed the other micro wind turbines. A multi-blade system is preferable for a micro wind turbine. Bourhis et al. [13] investigated the effect of blade solidity on micro-scale and low tip-speed ratio wind turbines. They varied the solidity by varying the blade chord length rather than the number of blades. To conclude, the best compromise between the maximum power coefficient, the cut-in wind speed, the mass of filament, and the stability of the wake is achieved for the rotor with a blade solidity of 1.25. Birajdar et al. [14] studied the effects of the TSR, angle of attack, rotor solidity, and number of blades on the aerodynamic performance of a small wind turbine. Their results indicated that $C_{P,max}$ was 0.5 at the optimum TSR and angle of attack of 7 and 4.5°, respectively. Moreover, the turbine with three blades had the optimal rotor solidity. Sudarma et al. [15] experimentally and numerically investigated the effect of the number of blades on the performance of a small HAWT with winglet blade tips. An increase in the number of blades was found to cause increases in the torque and output power. The presence of winglets increased the pressure on the blade surface and caused the concentration of wind flow at the blade tips, which resulted in improved rotor performance. Eltayesh et al. [16] investigated the effect of the number of blades on the performance of a small HAWT. They found that compared with a five-blade configuration and a six-blade configuration, a three-blade configuration resulted in 2% and 4% higher $C_{P,\max}$ values, respectively. An increase in the number of blades caused an increase in the torque and enabled the turbine to operate at a lower TSR. Zawadzki et al. [17] examined the effect of rotor solidity on the performance of a small HAWT. An increase in rotor solidity was discovered to lead to an increase in $C_{P,\max}$ but a slight decrease in the TSR. Chaudhary and Prakash [18] explored the effects of rotor solidity (ranging from 0.055 to 0.207) and the number of blades (ranging from 3 to 7) on rotor performance. They found that $C_{P,\max}$ increased with the number of blades, and that favorable performance was achieved only when rotor solidity was 0.055–0.085. Porto et al. [19] conducted experiments to investigate the effect of the number of blades on the performance of a HAWT. Their results indicated that a five-blade rotor outperformed a three-blade one; the five-blade rotor had higher static torque, which resulted in a shorter starting time and a higher C_P value (39%). Chaudhary and Roy [20] optimized the number of blades, rotor solidity, and TSR on the basis of blade element momentum theory. They found that $C_{P,\max}$ varied strongly with a change in the rotor solidity but weakly with a change in the number of blades. They concluded that a rotor with five blades and solidity of 5–10% would achieve C_P of 0.5 at a blade pitch angle of 3°. Vashkevitch et al. [21] obtained experimental data on the performance of a novel HAWT under various blade incidence angles. They found that the developed turbine exhibited high efficiency at the optimum blade incidence angle of 7.5°, with $C_{P,\max}$ being 0.538. Mayer et al. [22] investigated the starting performance of a HAWT under blade pitch angles of 0°–35°. Their results revealed that (1) the turbine exhibited $C_{P,\max}$ at a blade pitch angle of 0°, (2) the starting process of the turbine was characterized by a long idling period, and (3) the turbine's startup was best for a blade pitch angle of 20°. Kriswanto et al. [23] adopted the Taguchi method to optimize the performance of a HAWT. Their analysis of variance (ANOVA) results indicated that of all the investigated parameters, the airfoil had the strongest influence on the rotor power of the HAWT. The highest lift coefficient and lift-to-drag ratio were achieved with the SD7080 airfoil under angles of attack ranging from 0° to 20°. Although the blade pitch angle can affect the performance of a HAWT, its effect may be weaker than those of the airfoil and angle of attack. Kaya et al. [24] numerically studied the aerodynamic effects of the blade pitch angle on the performance of small HAWTs at different TSRs. Their results indicated that at low TSRs, a more downward blade pitch angle resulted in a higher C_P and a smaller thrust coefficient (C_T); however, at high TSRs, the effect of the blade pitch angle on C_P was the reverse. At low TSRs, a higher blade pitch angle resulted in the flow separation location being closer to the leading edge of the blade and the tip vortices being stronger.

The development of diffuser-augmented wind turbines (DAWTs) improving rotor performance began in the 1950s and has been a hot research topic since the Wind Energy Innovative Systems Conference of 1979. Many studies have indicated that DAWTs have advantages over other types of augmented wind turbines [2]. A diffuser or duct can generate separation regions behind it; thus, compared with a bare wind turbine, DAWTs produce low-pressure regions that draw in more wind at higher speeds past the rotors. Because wind's power is proportional to the cube of its speed, a slight increase in wind speed can considerably increase the power output of wind turbines. The performance of a DAWT depends on several factors, such as the diffuser shape, diffuser geometry, and rotor blade geometry. The diffuser can have different shapes, such as a nozzle or flange shape, and the geometric parameters of a diffuser include the rotor diameter, nozzle length, nozzle angle, diffuser length, diffuser angle, and flange height. Rahmatian et al. [25,26] optimized the design of converging-diverging ducts using the response surface method (RSM) and a genetic algorithm (GA) and investigated the effect of the duct diffuser on the aerodynamic performance of a micro HAWT. Their optimal duct design increased $C_{P,max}$ by a factor of 3.94 and reduced the noise level and dynamic forces behind the turbine. Wang and Chen [27] numerically investigated the effect of the number of blades on the performance of a converging-diverging ducted wind turbine. They found that a higher number of blades results in higher torque and a larger blade area for capturing wind energy; however, it also results in greater blockage and thus lower C_P. Therefore, using an appropriate number of blades is essential for achieving high wind turbine performance and efficiency. Asl et al. [28] studied the effects of the number of blades, blade geometry, and angle of attack on the rotational speed of a converging-diverging ducted wind turbine. Their results indicated that the rotational speed (1) decreased with an increase in the number of blades, (2) decreased with an increase in the width of the top blades, and (3) increased with an increase in the angle of attack.

Chen et al. [29] investigated the effect of a flanged diffuser on the rotor performance of micro wind turbines under different rotor solidity values. This study is motivated by micro-HAWTs being suitable for moving vehicle applications, because high-speed and stable wind is easily generated as the vehicle moves. The results showed that the use of a flanged diffuser resulted in a substantial enhancement of rotor performance, which was predominantly influenced by rotor solidity. Rotor solidities of 30% and 40% resulted in the highest power outputs, whereas a rotor solidity of 60% resulted in the highest torque output. The study mentioned above also revealed that the investigated wind turbine exhibited low torque and high rotor rotational speed. Chen et al. [30] evaluated the aerodynamics of a ducted micro wind turbine with large-tip untwisted blades. Their results suggested that a rotor solidity of 60% resulted in high power and torque outputs at a relatively low rotational speed; thus, this rotor solidity value is suitable for micro wind turbines.

As mentioned above, much of the previous literature examined parameter effects on rotor performance by one-factor-at-a-time investigations, implying that the conclusions were drawn under specific experiment conditions, resulting in bias. Consequently, the conclusions could differ if the experiment conditions are different. For example, Duquette et al. [11] found that an increase in the number of blades did not cause an improvement in rotor performance; the aerodynamic efficiency and power even decreased when the number of blades was increased to 12. However, Sudarma et al. [15] and Porto et al. [19] concluded that an increase in the number of blades causes an increase in the power output of a wind turbine. Similarly, scholars have obtained differing results regarding the effect of rotor solidity on rotor performance. Considerable research has discovered that an increase in rotor solidity causes a substantial improvement in rotor performance; however, Chaudhary and Prakash [18] found that this effect was only observable under rotor solidity values of 0.005 to 0.085, with a further increase in rotor solidity resulting in a decrease in rotor performance. The differences in the conclusions of the aforementioned studies may have been caused by differences in their experimental conditions with the one-factor-at-a-time investigations. By contrast, the Taguchi method involves using an orthogonal array (OA) to design experimental conditions that enable the simultaneous systematic assessment of the effects of multiple relevant parameters on a certain quality [31]. In this method, the signal-to-noise (S/N) ratio is employed to evaluate quality and to achieve optimum quality with minimal variance [32]. Moreover, the Taguchi method is also known as robust parameter design owing to the finding of the optimum parameters, considering that quality may be affected by the design, the production, and environmental disturbance [31]. Additional information on this method is provided in the papers of Roy [33] and Ross [34]. Some studies have adopted the Taguchi method to optimize wind turbine design [23,35,36].

In previous studies of wind turbines installed on mobile vehicles, the rotor sizes investigated were relatively large. As a result, they needed to be installed on the vehicle's roof or hood, causing additional resistance and fuel consumption concerns. A micro wind turbine can be installed in front of or inside the engine compartment of a car without causing additional drag. The present study focused on optimizing the blade geometrical parameters of a ducted micro HAWT based on an existing flanged duct investigated by the corresponding author of this article. The results obtained can provide guidelines for the development of a micro wind turbine suitable for installation in a mobile vehicle. In a further study, the authors will use the obtained optimal rotor blade geometrical parameters to examine the optimization of a flanged converging-diverging duct. The rest of this paper is divided into four sections. Section 2 describes the parameter optimization process, Section 3 details the numerical model of this study, and Section 4 presents the numerical results. Finally, Section 5 provides the conclusions of this study and suggestions for the design of a ducted micro HAWT.

2. Taguchi Optimization Process

In this study, the blade geometry of a ducted micro HAWT was optimized using the Taguchi method. The control factors in this study were the number of blades n, rotor solidity σ, and blade pitch angle β (A, B, and C, respectively). Every control factor was set to three-level values. Wind turbines installed on vehicles must have a small rotor diameter. Therefore, a rotor diameter of 30 cm was selected in this study. Duquette and Visser [11] and Chen et al. [35,36] have suggested that when the rotor diameter is small, higher rotor solidity results in a higher $C_{\mathrm{P,max}}$ value. Of the rotors studied by Chen et al. [30], the rotor with 60% solidity exhibited the highest power. In the present study, the rotor solidity was set as 50%, 60%, and 70%. Chen et al. [30] also found that when the rotor diameter is small, a higher number of blades results in the generation of more power. Therefore, the number of blades was set as 8, 10, and 12 in this study. In addition, the blade pitch angle was set as 25°, 30°, and 35°. The control factors and their corresponding levels are summarized in Table 1. Given that a wind turbine may operate at various wind speeds, wind speeds of 10 and 16 m/s were regarded as noise factors to achieve a robust quality characteristic. The $C_{\mathrm{P,max}}$ value of the ducted micro HAWT was the objective quality to be maximized in this study. After determining the investigated control factors and their level numbers, the experimental conditions were arranged using an $L_9(3^4)$ OA and carried out by numerical simulation.

Table 1. Control factors and corresponding parameter values at each level.

Control Factor	Description	Level 1	Level 2	Level 3
A	Blade number	8	10	12
B	Rotor solidity	50%	60%	70%
C	Blade pitch angle	250	300	350

The simulated wind turbine was similar to the wind turbine used in experiments by Chen et al. [30]. Figure 1 displays the simulated micro HAWT with a flanged diffuser system. The flanged diffuser had an inlet radius of 15 cm, a length of 10 cm, a diffusion angle of 30°, and a flange height of 3 cm [Figure 1a]. The present study focused on the effects of blade geometry on rotor performance; therefore, the design of the flanged diffuser was not optimized. The cross-sectional profile of the rotor blade was an NACA 4415 airfoil. The blades of the simulated turbine were untwisted blades with a length of 12 cm, and β was varied from 25° to 35°; these blades were attached to a cone hub with a base diameter of 8 cm and a length of 6 cm [Figure 1b], which resulted in a rotor diameter of 30 cm. The assembled rotor was placed in the middle of the flanged diffuser [Figure 1c]. The required rotor solidity was achieved by adjusting the chord lengths of the blade tip and root.

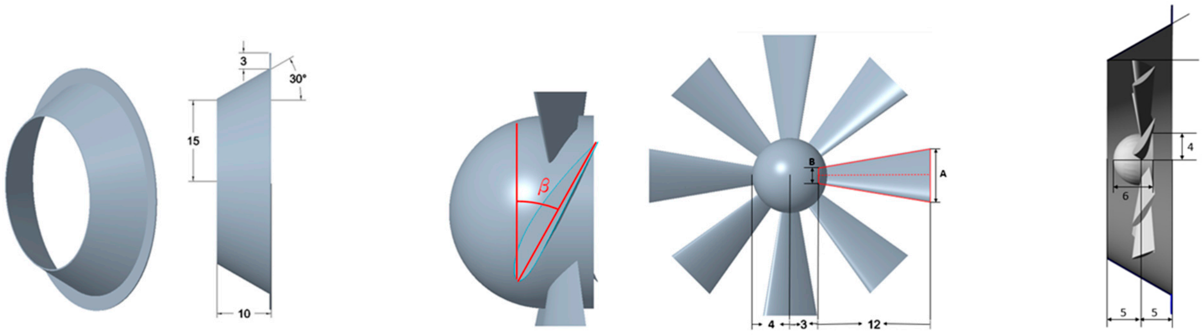

(**a**) (**b**) (**c**)

Figure 1. The dimensions of the flanged diffuser micro HAWT system: (**a**) flanged diffuser; (**b**) cone hub and rotor blade; (**c**) assembled micro HAWT. (Unit: cm).

Table 2 presents the chord lengths of the blade tip and root [denoted as *a* and *b* in Figure 1b, respectively] for different numbers of blades and rotor solidities. The blade profiles of an eight-blade rotor with different solidities are displayed in Figure 2.

Table 2. The chord lengths of the blade tip and root for different blade numbers and rotor solidities.

Number of Blades	Rotor Solidity	Blade Tip (*a*)	Blade Root (*b*)
8 blades	50%	6.0 cm	1.8 cm
	60%	7.0 cm	2.1 cm
	70%	8.0 cm	2.5 cm
10 blades	50%	5.0 cm	1.2 cm
	60%	5.5 cm	1.7 cm
	70%	6.0 cm	2.0 cm
12 blades	50%	4.0 cm	1.0 cm
	60%	4.3 cm	1.2 cm
	70%	5.0 cm	1.6 cm

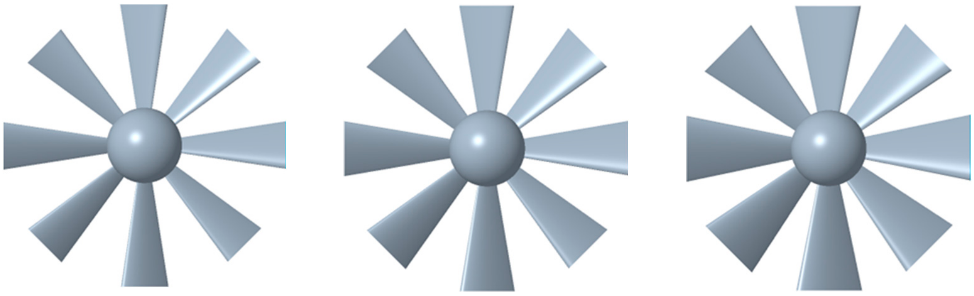

σ = 50% σ = 60% σ = 70%

Figure 2. The blade profiles of the 8-blade rotor for various rotor solidities.

Several dimensionless parameters discussed in subsequent sections are defined as follows. The power coefficient C_P and torque coefficient C_T of a wind turbine are expressed as follows:

$$C_P = \frac{T\omega}{\frac{1}{2}\rho A V^3} \tag{1}$$

$$C_T = \frac{T}{\frac{1}{2}\rho A V^2 R} \tag{2}$$

where T is the torque generated by the rotor, ω is the rotor's angular speed, ρ is the wind density, A is the rotor's swept area, R is the radius of the rotor, and V is the free-stream wind speed. In addition, the TSR is expressed as follows:

$$\mathrm{TSR} = \frac{R\omega}{V} \tag{3}$$

The expressions for these dimensionless parameters above can be referred to [25].

3. Numerical Model

In this study, the operation of a ducted micro HAWT in an open environment was simulated using the commercial computational fluid dynamics software FlowVision 3.12.04. The dimensions and boundary conditions of the three-dimensional computational domain are shown in Figure 3. Wind entered from the inlet on the left side of this domain at a speed of 10 or 16 m/s, encountered the wind turbine, and flowed out from the outlet on the right side. The dimensions of the computational domain were 20R, 9R, and 9R in the streamwise (x), transversal (y), and vertical (z) directions, respectively. The wind turbine was located at the center of the longitudinal cross-section of the computational domain, namely, at a distance 2.7R downstream of the inlet.

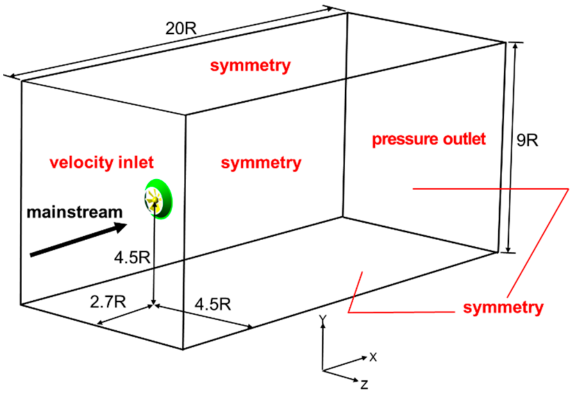

Figure 3. The dimensions of the computational domain and the boundary conditions set.

3.1. Governing Equations and Boundary Conditions

The governing equations for the operation of a wind turbine under incompressible turbulent airflow are continuity and momentum equations, as well as a turbulent model. The Reynolds-Averaged Navier–Stokes (RANS) method was implemented to model the flow.

With regard to the boundary conditions, the left inlet was set as the velocity inlet. The right outlet was the pressure outlet with a static pressure of 101,325 Pa. The surfaces of the wind turbine and the walls of the flanged diffuser were assumed to be nonslip adiabatic walls. The perimeter boundaries of the computational domain were set to be symmetry conditions to simulate an open environment. The boundary conditions are summarized in Table 3.

Table 3. Boundary conditions of the numerical model.

Boundaries	Boundary Condition Type and Specified Parameters
Left inlet	Velocity inlet condition • Velocity profile: the one-seventh power law • Inlet temperature: 293 K
Right outlet	Pressure outlet condition • Static pressure: 101,325 Pa
Surfaces of the micro HAWT and flanged diffuser	Non-slip adiabatic wall condition
Perimeter boundaries	Symmetry condition

3.2. Grid Generation

In FlowVision 3.13.04, a locally adaptive approach based on the Cartesian coordinate system is used for computational grid generation, and the sub-grid geometry resolution (SGGR) approach is employed to resolve computer-aided design (CAD) geometries. To generate a grid mesh, an initial Cartesian grid (level of grid adaptation = 0) is created, and this grid is then refined through subsequent adaptations [level of grid adaptation (n) = 1, 2,. . .]. The initial grid is established using a simple Cartesian rectangular grid, which the program automatically splits into solid and fluid cells during the computation process. Consequently, cells that contain data regarding the CAD geometries' boundaries are created. To eliminate noncomputed volumes, the program performs Boolean subtraction on rectangular cells located near the computational domain's border, which results in the creation of polygonal cells with diverse shapes.

After the initial grid is generated, it can be refined for accurately capturing the geometric details and flow near the boundaries. Grid refinement is a dynamic process that can be triggered during simulation. In FlowVision, the grid refinement feature enables the user to refine the grid mesh on the basis of boundary surfaces, user-defined regions within the computational domain, and parameters such as pressure gradients, velocity gradients, and vorticity. The resultant grid accurately captures flow characteristics with optimal efficiency. Grid refinement is performed by splitting every edge of each cell of the initial grid into 2^n smaller equal edges so that each initial cell is divided into $2^n \times 2^n \times 2^n$ cells, where n represents the level of grid adaptation (Figure 4). Details on the SGGR approach and grid refinement are provided in the study of Aksenov et al. [37] and the user guide of FlowVision [38].

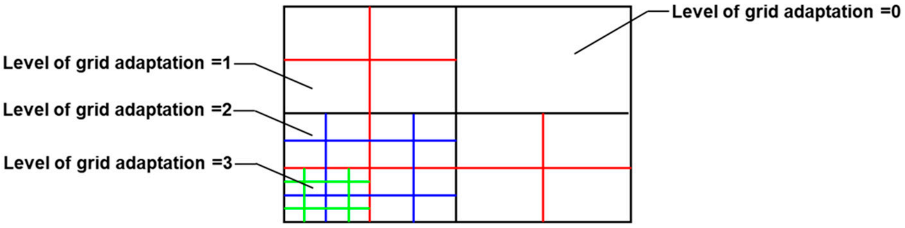

Figure 4. The levels of splitting the computational grids in FlowVision.

3.3. Validation of the Numerical Model

The grid independence, turbulence model, and accuracy of the developed numerical model were validated by comparing the results obtained using this model with the experimental results of Chen et al. [30]. A second-order upwind scheme was used for spatial discretization, and the SIMPLEC algorithm was adopted for pressure–velocity coupling. The iterative criterion was that the residuals for continuity, momentum, the turbulent kinetic energy (k), and the dissipation rate of k (ε) had to be smaller than 10^{-5}. Because Chen et al. [30] conducted their experiments in a wind tunnel, the original perimeter boundary conditions of the computational domain were changed from symmetric boundaries to nonslip adiabatic wall boundaries. In addition, the simulated wind turbine was moved 1 m downstream of the entrance to adhere completely to the configuration of the wind tunnel experiments of Chen et al. [30]. In these experiments, the highest power output was achieved with an eight-blade wind turbine having a blade pitch angle of 30° and rotor solidity of 60% at a torque of 0.2 N-m applied on the turbine. Therefore, the aforementioned configuration was adopted to compare the numerical calculations with the experimental results.

To ensure that the computational results were unaffected by the number of grids, the grid independence was investigated. In the simulations, the grids around the duct and rotor were refined, whereas the initial grid mesh for the other areas was kept unchanged. The grid distribution of the computational domain is shown in Figure 5. Figure 5a illustrates the meshes of the entire computational domain in three dimensions, and Figure 5b,c displays enlarged meshes for the duct and rotor, respectively. The grid adaptation level for the meshes surrounding the duct was 1. Its grid refinement divided the edges of the initial grid cell by half [Figure 5b]. Furthermore, the grid adaptation level for the meshes surrounding the rotor was 2, and the grid refinement divided the edges of the cell of grid adaptation level 1 further by half [Figure 5c]. Subsequently, the simulated wind turbine's rotational speed was calculated using 0.66 million, 1.37 million, 1.50 million, and 1.86 million grids under a torque of 0.2 N-m on the wind turbine and wind speed of 10 m/s. The standard k–ε turbulence model (KES model) was used at this stage. Table 4 presents the simulated rotational speeds obtained with different numbers of grids and the experimental rotation speed obtained by Chen et al. [30]. The experimental rotation speed was 1194 RPM, and the simulated rotational speeds obtained with 0.66 million, 1.37 million, 1.50 million, and 1.86 million grids were 1050, 1098, 1136, and 1143 RPM, respectively; thus, the corresponding errors were 12.1%, 8.0%, 4.8%, and 4.3%, respectively. The grid independence evaluation revealed that a mesh with 1.50 million grids was sufficient for accurately simulating the performance of the considered wind turbine. A further increase in the number of meshes had a limited positive effect on the accuracy. Therefore, a mesh with 1.50 million grids was used for the subsequent computations in this study.

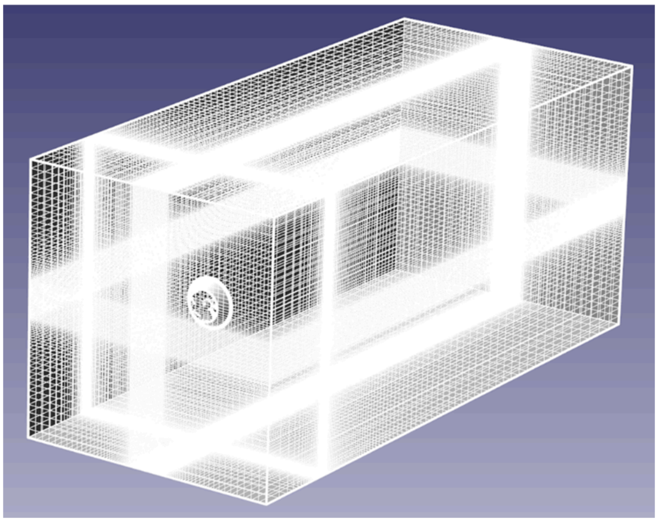

(**a**) Entire computational domain

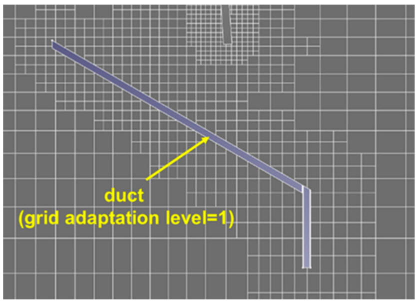

(**b**) Enlarged view of the duct

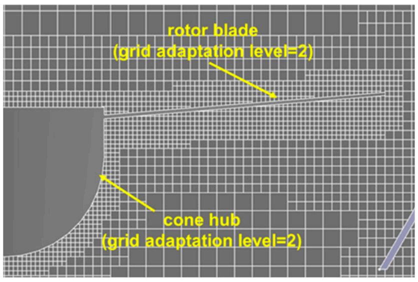

(**c**) Enlarged view of the rotor

Figure 5. Grid distribution of the computational domain.

Table 4. Grid-independent validation.

	RPM	**Related Error**
Experiment	1194	
0.66×10^6 grids	1050	12.1%
1.37×10^6 grids	1098	8.0%
1.50×10^6 grids	1136	4.8%
1.86×10^6 grids	1143	4.3%

To determine the most appropriate turbulence model for simulating wind turbine flow fields, three turbulence models provided by FlowVision were evaluated: the KES model, the Menter shear stress transport (SST) model, and the modified k–ε model of FlowVision (KEFV model). The SST model is a combination of the k–ε and k–ω models. For simulations conducted with the SST model, the equations of the k–ω model were applied in the wall regions, and the equations of the k–ε model were applied in the regions far from the walls. As detailed in Table 5, the simulated rotational speeds obtained with the KES, SST, and KEFV models were 1136, 1126, and 1117 RPM, respectively. The rotational speeds obtained with the three turbulence models were close; however, the speed obtained using the KES model was closest to the experimental result. Therefore, this model was employed in the subsequent numerical simulations.

Table 5. Turbulent model validation.

Turbulent Model	RPM	Related Error
Experiment	1194	
KES	1136	4.8%
SST	1126	5.7%
KEFV	1117	6.4%

Subsequently, the rotor was subjected to various torques to replicate the loads of a generator exerted on the wind turbine to determine the C_P–TSR relationship. Figure 6 illustrates the C_P–TSR relationship derived using 1.50 million grids and the KES model as well as the corresponding experimental data. For TSR values below 1.6, the calculated C_P values were slightly lower than the experimental values; however, the difference was not major. When the TSR exceeded 1.6, the difference between the calculated and experimental C_P values increased. Nevertheless, the trends in the simulated C_P closely mirrored those of the experimental C_P, even at high TSR values. The simulated and experimental $C_{P,\max}$ values were 0.569 and 0.597, respectively, with the error being 4.7%.

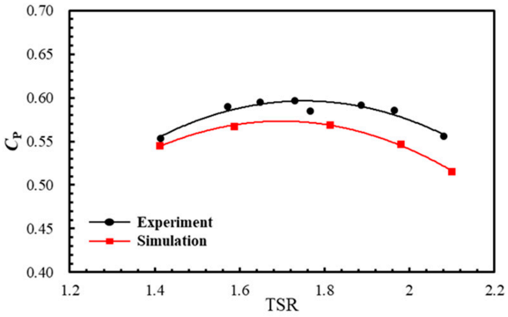

Figure 6. Comparison of the C_P–TSR relationship between the simulations and experiments.

In the KES model, the turbulent kinetic energy k and its dissipation rate ε are expressed as follows:

$$\rho u_i \frac{\partial k}{\partial u_i} = \frac{\partial}{\partial x_i}\left[\left(\mu + \frac{\mu_t}{\sigma_k}\right)\frac{\partial k}{\partial x_i}\right] + G_k + G_b + \rho\varepsilon \tag{4}$$

$$\rho u_i \frac{\partial \varepsilon}{\partial u_i} = \frac{\partial}{\partial x_i}\left[\left(\mu + \frac{\mu_t}{\sigma_{k\varepsilon}}\right)\frac{\partial \varepsilon}{\partial x_i}\right] + G_{1\varepsilon}\frac{\varepsilon}{k}(G_k + G_{3\varepsilon}) - G_{2\varepsilon}\rho\frac{\varepsilon^2}{k} \tag{5}$$

Details on the derivations of Equations (6) and (7) can be obtained from the study of Versteeg and Malalasekera [39].

4. Results and Discussion

4.1. Taguchi Analysis

According to the experimental conditions in the $L_9(3^4)$ OA, simulations were performed at wind speeds of 10 and 16 m/s. The operation of the considered wind turbine was simulated under various applied loads in every experimental trial to obtain the C_P–TSR relationship (Figure 7). The numerals in the legends of Figure 7 indicate the number of blades, rotor solidity, and blade pitch angle in sequence. Comparing Figure 7a,b, the results show that the C_P–TSR trends at wind speeds of 10 m/s and 16 m/s were similar. The configurations with the highest $C_{P,\max}$ at these two wind speeds were eight blades, 60% solidity, and a 30-degree pitch angle, and the $C_{P,\max}$–TSR were 0.432–1.2 and 0.431–1.3 for the wind speeds of 10 m/s and 16 m/s, respectively. On the basis of the results depicted in Figure 7, the $C_{P,\max}$ values at wind speeds of 10 and 16 m/s were determined and averaged. Subsequently, the standard deviations S and S/N ratios were calculated. The standard deviation was defined as follows:

$$S = \sqrt{\frac{\sum_{i=1}^{N}(y_i - \overline{y})^2}{N}} \tag{6}$$

where y_i is the ith measurement, $\overline{y}$ is the mean, and N is the total number of measurements. Because the goal of this study was to maximize the power coefficient of the wind turbine, the quality characteristic of the "larger the better" was considered. For this quality characteristic, the S/N ratio is obtained using the following equation [33]:

$$S/N = -10 \times \log \frac{1}{N}\left(\sum_{i=1}^{N}\frac{1}{y_i^2}\right) \tag{7}$$

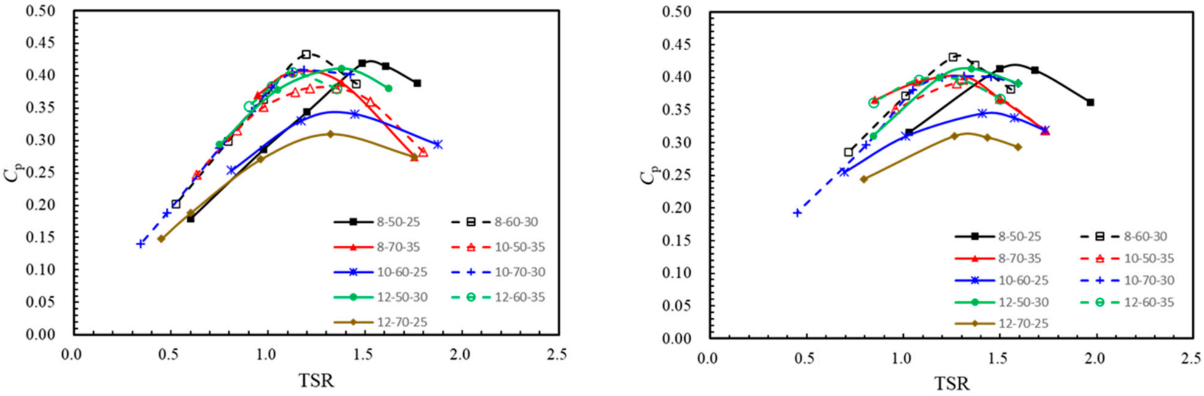

(**a**) V = 10 m/s (**b**) V = 16 m/s

Figure 7. The C_P–TSR relationship for every experimental trial at wind speeds of 10 m/s and 16 m/s.

Table 6 presents the numerical results obtained for the experimental conditions in the $L_9(3^4)$ OA. The numbers in the left half of this table indicate the factor level in the experimental trial.

Table 6. Numerical results according to $L_9(3^4)$ OA.

Exp.	*A*	*B*	*C*	Ave. $C_{P,\max}$	*S*	*S*/*N*
1	1	1	1	0.418	0.004	−7.587
2	1	2	2	0.432	0.001	−7.300
3	1	3	3	0.404	0.001	−7.872
4	2	1	3	0.386	0.006	−8.281
5	2	2	1	0.343	0.002	−9.307
6	2	3	2	0.394	0.008	−8.093
7	3	1	2	0.412	0.001	−7.702
8	3	2	3	0.402	0.005	−7.927
9	3	3	1	0.310	0.000	−10.173

4.1.1. Effects of Individual Control Factors

Derived from the outcomes presented in Table 4, Figure 8 illustrates the effect of the level of each control factor on the S/N ratio. In Figure 8, A_1 denotes level 1 of factor A, and the other notation similarly corresponds to different levels of the various factors. The results displayed in Figure 8 indicate that when the level of factor A (number of blades) was increased from 1 to 2, the S/N ratio notably decreased from −7.59 to −8.56. Moreover, when the level of factor A was further increased to 3, the S/N ratio further decreased to −8.60. One possible reason for the aforementioned results is that under high rotor solidity (50%–70% in this study), an excessive number of blades obstruct the wind as it encounters the wind turbine, thus reducing the airflow through the rotor blades and consequently decreasing the captured wind energy. The effect of the level of factor B (rotor solidity) on the S/N ratio closely resembled that of the level of factor A. When the level of factor B was increased from 1 to 2 and 3, the S/N ratio decreased from −7.86 to −8.18 and −8.71, respectively. The rotor solidity of a wind turbine is closely linked to the turbine's power output. A certain rotor solidity value optimizes the efficiency of wind energy extraction. Excessively high rotor solidity may lead to blade blur, thereby reducing the airflow through the blades and the captured wind energy [30]. When the level of factor C (blade pitch angle) was increased from 1 to 2, the S/N ratio increased from −9.02 to −7.77; however, when the level of factor C was changed to 3, the S/N ratio decreased to −8.03. These results were obtained because increasing the blade pitch angle causes an increase in the lift force acting on the blades and thus enhances the rotor performance; however, an excessive blade pitch angle can cause the blade to stall, thereby decreasing the rotor performance. On the basis of the results depicted in Figure 8, the preliminarily determined optimum control factor configuration (that achieving the highest S/N ratio) was identified as $A_1B_1C_2$ (i.e., a rotor with eight blades, solidity of 50%, and a blade pitch angle of 30°), and the worst control factor configuration (lowest S/N ratio) was identified as $A_3B_3C_1$ (i.e., a rotor with 12 blades, solidity of 70%, and a blade pitch angle of 25°) as a benchmark for subsequent comparison.

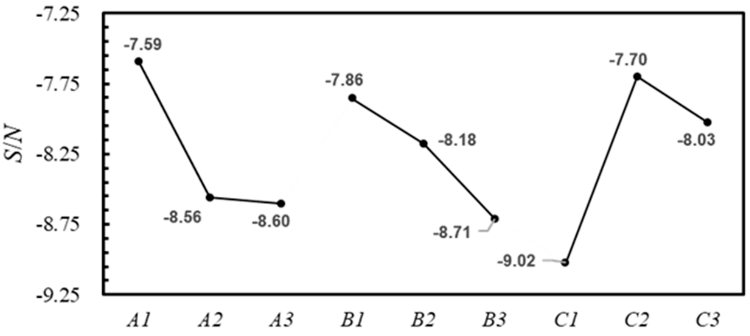

Figure 8. Effect of factor level on S/N.

ANOVA was conducted to evaluate the contribution of each factor to $C_{\mathrm{P,max}}$. Table 7 presents the ANOVA results for the average $C_{\mathrm{P,max}}$ values obtained at wind speeds of 10 and 16 m/s on the basis of the data presented in Table 4. In Table 7, SS indicates the sum of squares, DOF represents the degrees of freedom, $Var.$ represents the variance, F represents the F value obtained in the F test, and SS' is the pure sum of squares. The F test was performed to determine whether a factor had a significant effect on $C_{\mathrm{P,max}}$, with $F_{0.05}$ representing the F value at a 95% confidence level. Student's t-distribution was used to calculate relevant confidence intervals [40]. The F values of all three factors were larger than $F_{0.05}$, which indicated that these factors had significant effects on $C_{\mathrm{P,max}}$. The contributions of factors A, B, and C to $C_{\mathrm{P,max}}$ were 29.3%, 14.2%, and 39.3%, respectively; thus, of these factors, factor C had the strongest effect on $C_{\mathrm{P,max}}$.

Table 7. ANOVA on CP, max.

Factor	SS	DOF	$Var.$	F	$F_{0.05}$	SS'	Contribution (%)
A	0.0075	2	0.0038	15.460	3.982	0.0071	29.3%
B	0.0039	2	0.0020	8.003	3.982	0.0034	14.2%
C	0.0100	2	0.0050	20.438	3.982	0.0095	39.3%
Error	0.0027	11	0.0002	$S=$	0.0156		17.2%
Total	0.0241	17		At least 95% confidence level			100.0%

4.1.2. Interactions between Two Control Factors

The previous section discussed the effects of the levels of individual control factors on the S/N ratio and concluded the preliminary optimum parameter design is $A_1B_1C_2$. However, there may be interactions between factors that may alter the conclusion obtained by only considering individual control factors. In practice, examining the interactions between two factors is sufficient; interactions involving three or more factors can be disregarded. The two-factor interactions between factors A, B, and C are displayed in Figure 9. The interaction between factors A and B is illustrated in Figure 9a. A strong interaction was discovered between these factors. When the number of blades was eight (A_1), the S/N ratio increased and then decreased as the rotor solidity increased from 50% to 60% and 70% (B_1 to B_2 and B_3, respectively), respectively. When the number of blades was 12 (A_3), the S/N ratio consistently decreased with an increase in the rotor solidity. These results indicated that when the number of blades was relatively small (eight blades), a moderate solidity (60%) could achieve a better rotor performance; higher (70%) or lower (50%) rotor solidity resulted in lower rotor performance. However, when the number of blades was large (12 blades), the optimal rotor performance was achieved with the smallest rotor solidity of 50%. Figure 9a shows that when the interaction between factors A and B was considered, the highest S/N ratio was achieved for the control factor configuration A_1B_2.

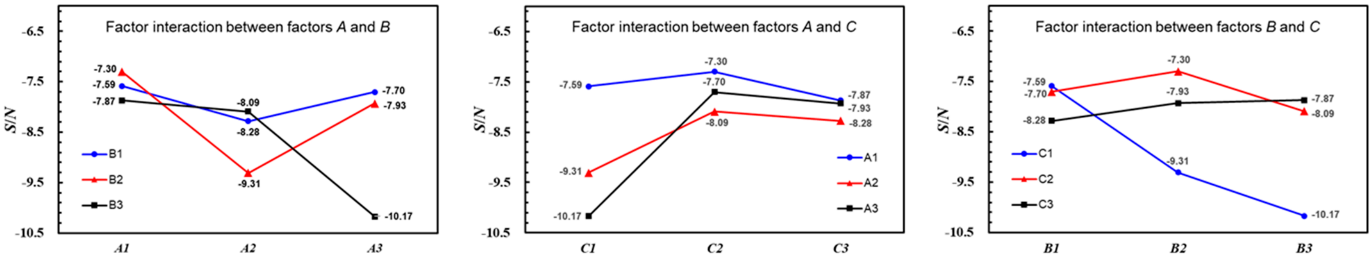

(**a**) (**b**) (**c**)

Figure 9. The effects of two-factor interactions on S/N ratio.

The interaction between factors A and C is illustrated in Figure 9b. Regardless of the number of blades (A_1 to A_3), the S/N ratio increased and then decreased as the blade pitch angle was increased from 25° to 30° and 35° (C_1 to C_2 and C_3, respectively), respectively. As mentioned, increasing the blade pitch angle can increase the lift force on the blades, thereby enhancing rotor performance; however, an excessive blade pitch angle can cause the blade to stall, thereby decreasing rotor performance. When the interaction between factors A and C was considered, the highest S/N ratio was achieved for the control factor configuration A_1C_2 [Figure 9b].

Figure 9c displays the interaction between factors B and C and indicates that strong and complex interactions existed between these factors. Under low rotor solidity of 50% (B_1), an increase in the blade pitch angle (C_1 to C_3) caused a decrease in the S/N ratio. By contrast, under high rotor solidity of 70% (B_3), an increase in the blade pitch angle caused an increase in the S/N ratio. Thus, the blade pitch angle required to achieve optimal rotor performance depended on the rotor solidity. This phenomenon is attributable to the mass flow rate of the airflow through a wind turbine being dependent on the rotor solidity, which affects the linear velocity of the airflow approaching the blades and the angle at which the airflow meets the blades (i.e., the angle of attack). Figure 9c indicates that when the interaction between factors B and C was considered, the highest S/N ratio was achieved for the control factor configuration B_2C_2. Thus, the results obtained under a consideration of interaction effects confirmed that the optimum control factor configuration included $A_1B_2C_2$, eight blades, 60% solidity, and a 30-degree pitch angle. The S/N ratio obtained under this configuration was -7.3, with the corresponding $C_{P,max}$ values being 0.432 and

0.431 under wind speeds of 10 and 16 m/s, respectively. The result of a high solidity of 60% agrees with the conclusion drawn by Chen's experimental results [30], e.g., a high rotor solidity value is suitable for micro wind turbines.

4.2. Analysis of Flow Velocity Distribution

According to Figure 7b, C_P nearly reached its maximum value for both the optimum and worst rotor geometries under a TSR of 1.265 and a wind speed of 16 m/s. Therefore, the flow velocity distribution was investigated at this TSR and wind speed. Figure 10 displays the velocity distribution of the entire flow fields from the side view (x–y plane) for the optimum and worst blade geometries. The results indicated that the flow field patterns were similar for the two blade geometries. As the airflow approached the ducted wind turbine, some of the airflow passed through the duct, whereas another part was diverted around it. The turbine inside the duct obstructed the airflow, causing a reduction in wind speed in front of the duct. However, the airflow that was diverted around the duct was accelerated. Similar flow field patterns were observed from the top view (x–z plane), a result not presented in this paper.

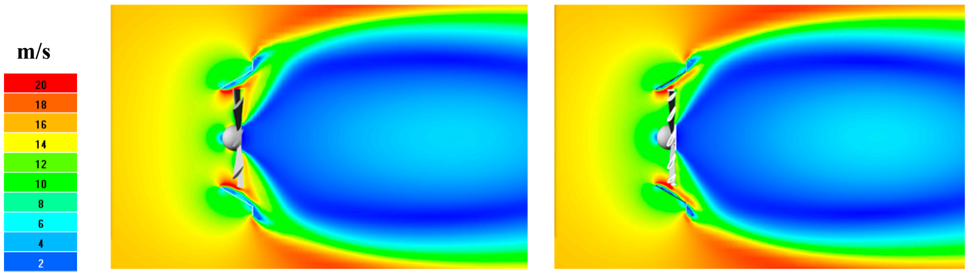

(**a**) Optimal blade geometry (**b**) Worst blade geometry

Figure 10. Velocity distributions in the x–y plane for the optimum and worst blade geometries.

Figure 11 represents the entire three-dimensional streamlines of the flow fields for the optimum blade geometry, and Figure 12 displays its two-dimensional streamlines in various x–z sections. After passing through the rotor, the airflow formed complex vortex structures with ellipsoidal shapes because of the rotating blades. These structures expanded downstream and widened because of the centrifugal force of the rotor. The width of the vortex structures did not increase beyond a distance of $3R$ from the rotor. Moreover, these structures became weak beyond a distance of $9R$ downstream from the rotor, and the flow eventually combined with the incoming outer airflow. In addition, Figure 12a shows that the vortex structures were apparent in the centerline section (z/R = 0). Moreover, reverse flows occurred inside the vortices. At z/R = 0.4, the sizes of the vortices decreased. One vortex exhibited shedding downstream, whereas the other vortex moved upstream, as shown in Figure 12b. At z/R = 0.6, the vortex structure almost disappeared, and the aforementioned vortices further developed upstream and downstream, respectively, as depicted in Figure 12c.

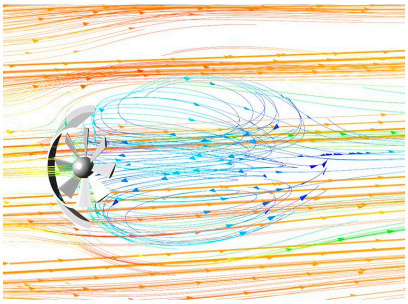

Figure 11. The streamline of the airflow passing through the wind turbine.

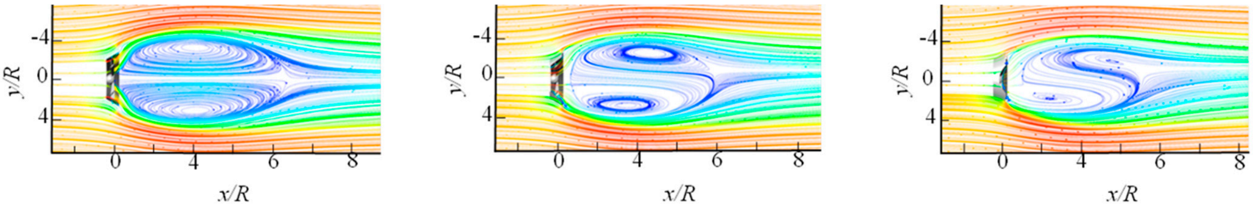

(**a**) $z/R = 0$ (**b**) $z/R = 0.4$ (**c**) $z/R = 0.6$

Figure 12. The vortex behind the rotor at various *x*–*z* sections.

The optimal design of the examined ducted micro HAWT comprised a rotor with eight blades, a solidity of 60%, and a blade pitch angle of 30°. The blades of an eight-blade rotor are spaced 45° apart; thus, the blades rotate 45° in one complete cycle. Figure 13 displays the airflow velocity distribution in the *x*–*y* plane around the ducted wind turbine for the optimum blade geometry under a TSR of 1.265, a wind speed of 16 m/s, and rotor rotation angles of 0°, 15°, and 30°. The trends in the flow field at the different rotation angles were approximately the same. As expected, flow separation occurred inside the diffuser and behind the flange. Large airflow velocities appeared near the blade tips, where the velocity distributions for the three rotation angles were only marginally different. The trends in the airflow velocity distribution were similar for the worst blade geometry. However, as illustrated in Figure 14, marginal variation in the airflow velocity magnitudes was found between the optimum and worst blade geometries. Thus, the airflow approaching the blades in these geometries had different linear velocities, which resulted in different angles of attack. The differences in the angle of attack affected the blade pressure distribution, as discussed in Section 4.3. When the airflow approached the duct inlet with a uniform velocity of 16 m/s, the wind speed was reduced because of the obstruction caused by the wind turbine inside the duct. The airflow velocities were nonuniformly distributed 5 cm in front of the duct inlet. The velocities for the optimum blade geometry were between 12 and 13.5 m/s, with the average velocity being 12.7 m/s. In addition, for the worst blade geometry, the velocities ranged between 11.3 and 12.5 m/s, with the average velocity being 12 m/s. When the airflow reached the duct inlet, the average velocities for the optimum and worst blade geometries decreased from 12.7 to 12 m/s and from 12 to 10.7 m/s, respectively. For the rotor with the optimum blade geometry, more air flowing into the duct should be related to the rotor solidity, which is closely related to the rotor power output. This implies that optimal rotor solidity exists such that more air particles pass through the blades, and thus more wind energy is captured. If the solidity is too small or too large, fewer air particles pass through the blades, and thus less wind energy is captured. Figure 14 indicates that as the airflow reached the duct inlet, its center velocity was reduced considerably by the rotor cone. The airflow was largely accelerated toward the duct wall, and its velocity then suddenly decreased near the wall because of flow separation.

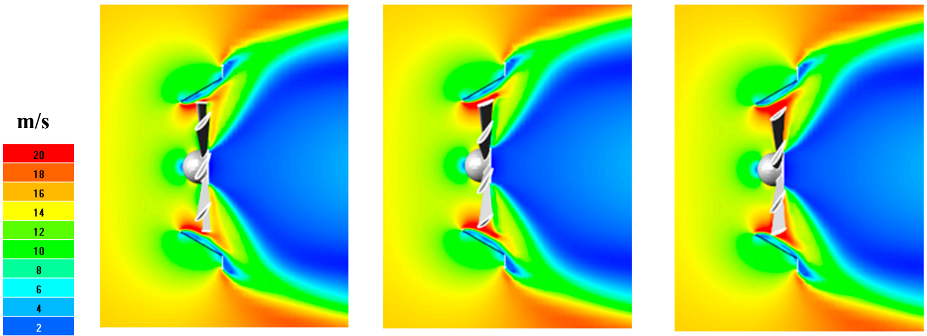

(**a**) 0 degrees (**b**) 15 degrees (**c**) 30 degrees

Figure 13. Velocity distributions in the vicinity of the ducted wind turbine at various rotation angles for the optimum blade geometry.

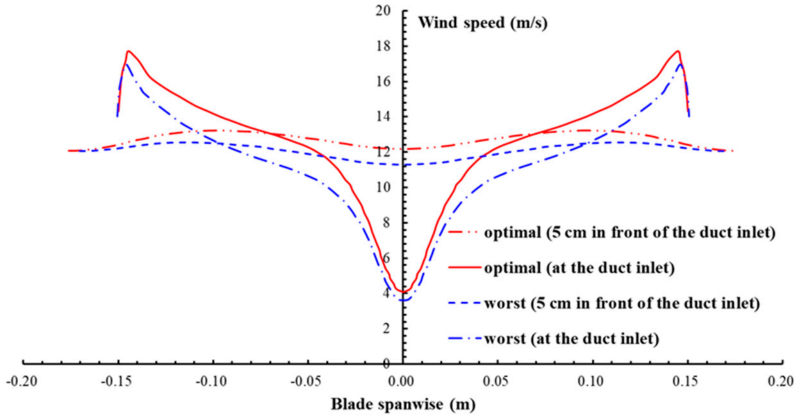

Figure 14. The velocity distributions near the duct inlet for the optimum and worst blade geometries.

Figure 15 depicts the axial velocity distribution in the y–z plane at the duct inlet and outlet for the optimum blade geometry. The airflow exhibited approximately symmetric movement at the duct inlet and outlet. Some of the kinetic energy of the airflow was transferred to the wind turbine; thus, the axial velocity behind the wind turbine decreased. Similar results were obtained for the worst blade geometry.

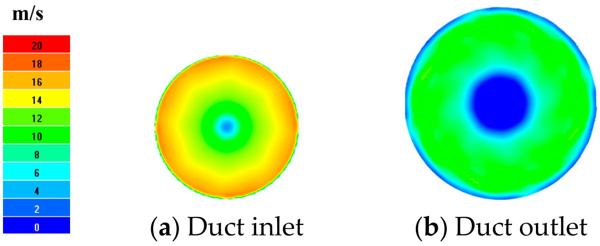

(**a**) Duct inlet (**b**) Duct outlet

Figure 15. Velocity distributions in the y–z plane at duct inlet and outlet for the optimum blade geometry.

4.3. Analysis of Pressure Distribution

Figures 16 and 17 display the pressure distributions on the windward and leeward sides, respectively, of the turbine blades for the optimum blade geometry at a TSR of 1.265, a wind speed of 16 m/s, and rotation angles of 0°, 15° and 30°. These figures reveal comparable pressure distributions at the different rotation angles. Similar results were obtained for the worst blade geometry; therefore, only the pressure distributions at a rotation angle of 0° are presented in this paper (Figure 18). Figures 16 and 17 indicate that the distribution of pressure on all blades was almost unaffected by the rotation angle. As shown in Figures 16 and 18a, the pressure on the blades on the windward side was positive in most regions, with negative pressure found near the tips and trailing edges of these blades. In addition, these two figures indicate that the distribution and magnitude of the pressures were not significantly different between the optimum and worst blade geometries. However, Figures 17 and 18b indicate negative pressure on most regions of the blades on the leeward side, with large negative pressure near the leading edge of each blade. The pressures were less negative for the worst blade geometry than those for the optimum blade geometry. Figures 16–18 also suggest that the pressure distribution varied in the spanwise direction. This phenomenon occurred because the velocity of the airflow approaching the blades varied with the blade spanwise location (Figure 14), which led to variation in the angle of attack, and thus the pressure distribution, in the spanwise direction. In addition, the pressure distribution varied in the chordwise direction because of the different curvatures of the NACA4415 airfoil. Additional details regarding the pressure distribution on the blades are provided in the following text.

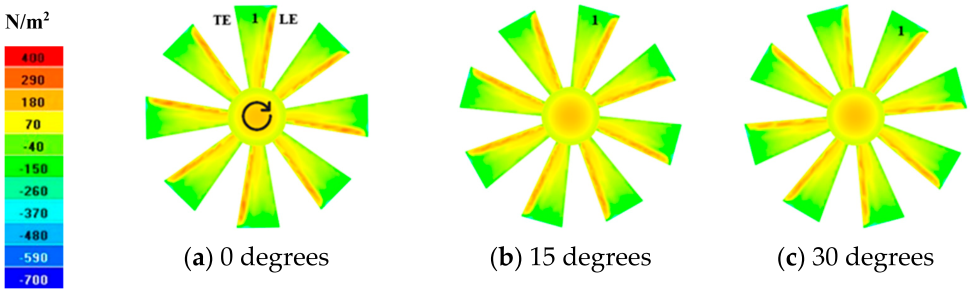

(**a**) 0 degrees (**b**) 15 degrees (**c**) 30 degrees

Figure 16. Pressure distribution on the windward side of turbine blades for the optimum blade geometry.

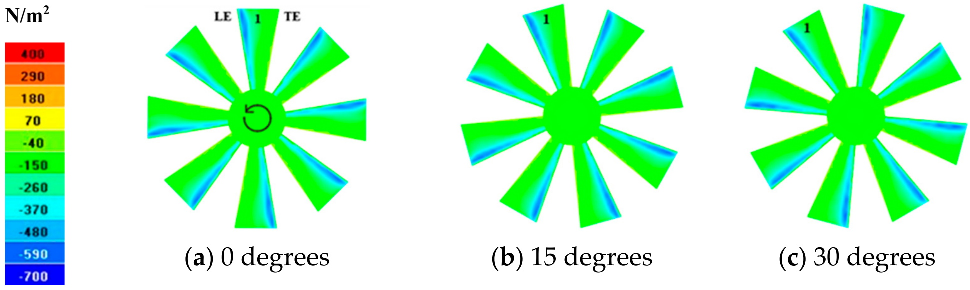

(**a**) 0 degrees (**b**) 15 degrees (**c**) 30 degrees

Figure 17. Pressure distribution on the leeward side of turbine blades for the optimum blade geometry.

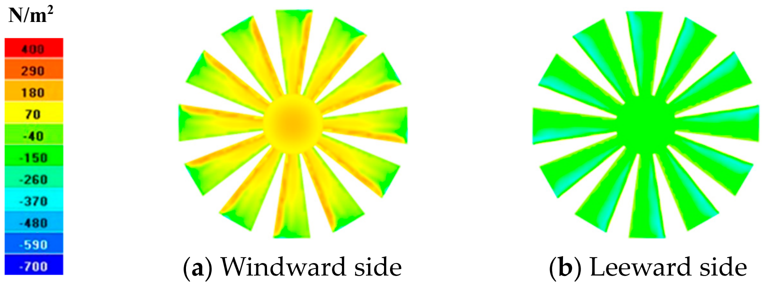

(**a**) Windward side (**b**) Leeward side

Figure 18. Pressure distribution on turbine blades for the worst blade geometry (0 degrees).

4.3.1. Pressure Distribution on the Turbine Blades for the Optimum Blade Geometry

Figure 19 displays the pressure distribution in the chordwise direction of a blade in different spanwise sections for the optimum blade geometry. The pressure distribution on the windward sides of the blades is discussed first. Near the blade root (r/R = 0.333), most regions on the windward side of the airfoil experienced high positive pressure [Figure 19a], where r is the distance from the cone hub in the radial direction. In the vicinity of the leading edge of the blades, the pressure was high and positive and decreased toward the trailing edge, where a small region of negative pressure occurred. Towards the blade tip, for example, at r/R = 0.8 [Figure 19b], the positive pressure was high only near the leading edge, and the pressures on most of the windward side were lower than that at r/R = 0.333. At r/R = 0.933, the pressure was mostly negative except near the leading edge [Figure 19c]. Negative pressure on the windward side of an airfoil hinders the generation of lift force, which limits the power output because little torque is generated. It is crucial to produce a large lift near the blade tip for a large power output, since it generates a large amount of torque. However, the results shown in Figure 19 indicate that the airfoil pressure distributions on the windward side became less positive and more negative closer to the blade tip. Twisting blades can modify the angle of attack of the airflow approaching the blades and thus enhance the lift force generated. Therefore, to increase a ducted micro HAWT's power output, twisted blades are suggested to further increase the torque output at the blade tip.

The pressure distribution on the leeward side of the blades is described in the following text. The pressure on the leeward sides was negative, and the distribution of this pressure was similar at different spanwise locations, as shown in Figures 17 and 19. The pressure was negative and high on the forward region of the airfoil; the maximum negative pressure occurred near the airfoil's maximum thickness, and the pressure was less negative toward the trailing edge.

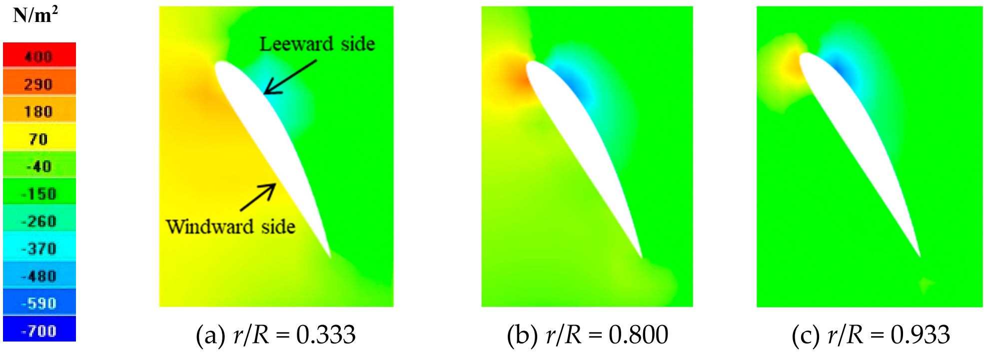

(a) r/R = 0.333 (b) r/R = 0.800 (c) r/R = 0.933

Figure 19. Pressure distributions along the airfoil at different blade spanwise sections for the optimum blade geometry.

4.3.2. Pressure Distribution on the Turbine Blades for the Worst Blade Geometry

Figure 20 depicts the pressure distribution along the airfoil in different spanwise sections of the blades for the worst blade geometry. A comparison of Figures 19 and 20 indicates that the pressure distribution on the windward side did not differ considerably between the optimum and worst blade geometries. The reason for this result is that although the flow velocities approaching the turbine blades [Figure 14] and the blade pitch angles in the two geometries were different, the effect of the angle of attack on the pressure distribution is small because of the small curvature of the airfoil on the windward side. As a result, the pressures on the whole windward side of the blades between the optimum and worst blade geometries did not differ very much, as also shown in Figures 16 and 18a.

The pressure on the leeward side of the turbine blades was negative, and the pressure distribution was similar at different spanwise locations, as shown in Figures 18b and 20. High negative pressure appeared in the forward region of the airfoil, and the pressure became less negative toward the trailing edge. The curvature of the airfoil was relatively high on the leeward side; thus, the effect of the angle of attack on pressure distribution was strong on this side. Consequently, the pressure distribution on the leeward side of the blades differed considerably between the worst and optimum blade geometries. In addition, the pressure on the leeward side of the blades was more negative for the optimum blade geometry than for the worst blade geometry.

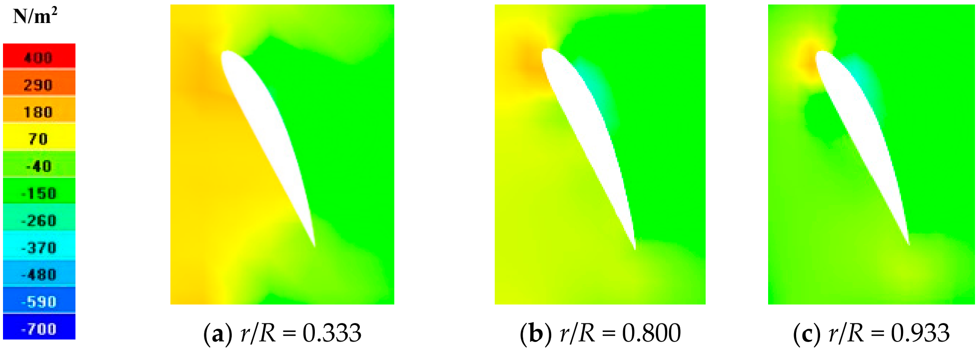

(**a**) r/R = 0.333 (**b**) r/R = 0.800 (**c**) r/R = 0.933

Figure 20. Pressure distributions along the airfoil at different blade spanwise sections for the worst blade geometry.

In summary, the pressure on the windward side of the blades was positive, whereas that on the leeward side was negative. Thus, the windward side of the blades is the pressure surface, whereas their leeward side is the suction surface. The pressure difference between these two sides results in the generation of lift force and thus torque for driving the rotation of the turbine blades. The rotor generated higher torque and thus higher power under the optimum blade geometry than under the worst blade geometry, because the pressure difference between the windward and leeward sides of the blades was greater under the optimum blade geometry.

The C_T–TSR relationships for the optimum and worst blade geometries are presented in Figure 21. The C_T is relative to the pressure difference between the windward and leeward sides of turbine blades. This figure shows that at low STR, the difference between the C_T of the optimum and worst geometries was not too much. The reason is that at low rotation, the effect of pressure distribution was not significant, and therefore, the pressure difference between these two blade geometries was not large. Up to a certain TSR, the optimum blade geometry had significantly higher CT than the worst one. The $C_{T,max}$ of 0.43 was achieved at a TSR of 1.2 for the optimum blade geometry, whereas the $C_{T,max}$ for the worst blade geometry was 0.31 at a TSR of 1.3. The $C_{T,max}$ for the optimum blade geometry is 38.7% higher than that for the worst.

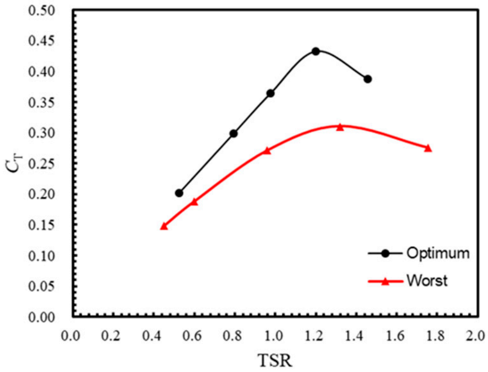

Figure 21. The C_T–TSR relationships for the optimum and worst blade geometries.

5. Conclusions

This numerical study optimized the blade geometry of a ducted micro HAWT through the Taguchi method to improve the rotor performance. The investigated rotor blades were untwisted with an NACA 4415 airfoil. Taguchi optimization can systematically and comprehensively investigate the parameter effects and avoid the bias caused by one-factor-at-a-time investigations. The numerical results were compared with the experimental results of Chen et al. [30] to examine the reliability of the numerical model. The relative error in $C_{P,max}$ was approximately 4.7%, indicating the developed model was reliable. The blade geometrical parameters investigated included the number of blades, rotor solidity, and blade pitch angle. The optimum parameter design included 8 blades, 60% solidity, and a 30° pitch angle, and the achieved $C_{P,max}$ was 0.432 at a TSR of 1.2, which was 39.4% higher than that obtained with the worst blade geometry. The optimum result of a high solidity of 60% confirmed the conclusion drawn from Chen's experiments [30], e.g., a high rotor solidity value is suitable for micro wind turbines. Of the three control factors, the blade pitch angle was found to have the most significant effect on the rotor's power output. In addition, strong factorial interactions were observed, implying that individually investigating wind turbine blade geometrical parameter effects potentially caused improper optimization.

The airflow aerodynamic characteristics were also discussed. After passing this wind turbine, airflow formed complex ellipsoidal vortex structures because of the rotor's rotation. Compared to the rotor with the worst blade geometry, the optimum rotor blade geometry could draw more airflow into the duct, and its pressure difference between the windward and leeward sides of the blades was greater, exhibiting higher $C_{P,\max}$. In addition, the optimum blade geometry achieved a $C_{T,\max}$ of 0.43 at a TSR of 1.2, which was 38.7% higher than the worst one. However, the untwisted blades considered in this study exhibited low torque near their tips; therefore, twisted blades should be used for further increasing the torque generated at the blade tips to achieve higher power output for the rotor.

In pursuit of sustainability and the mitigation of global warming impacts, nations across the globe are increasingly adopting green energy alternatives to conventional fossil fuels. Wind energy stands out as a pivotal component of green energy solutions due to its renewable and limitless nature. This study optimized the rotor blade geometry and provided some insight into the influence of blade geometrical parameters on rotor performance, thereby enhancing the efficiency of wind energy utilization and contributing to sustainable development goals (SDGs) like SDG 7 (affordable and clean energy).

Author Contributions: Conceptualization, T.-Y.C.; Methodology, K.O. and T.-Y.C.; Software, K.O. and J.-J.Y.; Validation, K.O. and T.-Y.C.; Formal analysis, K.O. and T.-Y.C.; Investigation, K.O. and T.-Y.C.; Data curation, J.-J.Y.; Writing—original draft, K.O.; Writing—review and editing, T.-Y.C.; Visualization, K.O. and J.-J.Y.; Supervision, T.-Y.C. All authors have read and agreed to the published version of the manuscript.

Funding: This research received no external funding.

Institutional Review Board Statement: Not applicable.

Informed Consent Statement: Not applicable.

Data Availability Statement: The data supporting this study's findings are available upon request from the corresponding author upon reasonable request.

Acknowledgments: The authors gratefully acknowledge the constructive comments given by the anonymous reviewers.

Conflicts of Interest: The authors declare that they have no known competing financial interests or personal relationships that could have appeared to influence the work reported in this paper. This research did not receive any specific grant from funding agencies in the public, commercial, or not-for-profit sectors.

References

1. Arumugam, P.; Ramalingam, V.; Bhaganagar, K. A pathway towards sustainable development of small capacity horizontal axis wind turbines—Identification of influencing design parameters & their role on performance analysis. *Sustain. Energy Technol. Assess.* **2022**, *44*, 101019. [CrossRef]
2. Al-Quraishi, B.A.J.; Asmuin, N.Z.B.; Bin Mohd, S.; Al-Wahid, W.A.A.; Mohammed, A.N.; Didane, D.H. Review on diffuser augmented wind turbine (DAWT). *Int. J. Integr. Eng.* **2019**, *11*, 178–206. [CrossRef]
3. Kassa, B.Y.; Baheta, A.T.; Beyene, A. Current trends and innovations in enhancing the aerodynamic performance of small-scale, horizontal axis wind turbines: A review. *ASME Open J. Eng.* **2024**, *3*, 031001. [CrossRef]
4. Chaudhary, M.K.; Prakash, S. New airfoils for microhorizontal-axis wind turbines. *J. Eng. Res.* **2022**, *10*, 230–245. [CrossRef]
5. Yossri, W.; Ayed, S.B.; Abdelkefi, A. Airfoil type and blade size effects on the aerodynamic performance of small-scale wind turbines: Computational fluid dynamics investigation. *Energy* **2021**, *229*, 120739. [CrossRef]
6. Mostafa, N.H.; Talaat, M.; Ibrahim, M.M. Performance analysis and design a small horizontal axis wind turbine. Comprehensive Development of the Sinai Peninsula. In Proceedings of the 1st Annual Conference, Sharm El–Sheikh, Egypt, 26–28 December 2014.
7. Suresh, A.; Rajakumar, S. Design of small horizontal axis wind turbine for low wind speed rural applications. *Mater. Today Proc.* **2020**, *23*, 16–22. [CrossRef]
8. Abdelghany, E.S.; Sarhan, H.H.; Alahmadi, R.; Farghaly, M.B. Study the Effect of Winglet Height Length on the Aerodynamic Performance of Horizontal Axis Wind Turbines Using Computational Investigation. *Energies* **2023**, *16*, 5138. [CrossRef]
9. Roy, S.; Das, B.; Biswas, A. Effect of leading-edge protrusion shapes for passive flow control measure on wind turbine blades. *Ocean Eng.* **2023**, *269*, 113688. [CrossRef]

10. Duquette, M.M.; Visser, K.D. Numerical implications of solidity and blade number on rotor performance of horizontal-axis wind turbines. *J. Sol. Energy Eng. Trans.-ASME* **2003**, *125*, 425–432. [CrossRef]
11. Duquette, M.M.; Swanson, J.; Visser, K.D. Solidity and blade number effects on a fixed pitch, 50W horizontal axis wind turbine. *Wind Eng* **2003**, *27*, 299–316. [CrossRef]
12. Leung, D.Y.C.; Deng, Y.; Leung, M.K.H. Design optimization of a cost-effective micro wind turbine. *Proc. World Congr. Eng.* **2010**, *2*, 988–993.
13. Bourhis, M.M.; Ravelet, F.; Pereira, M. Experimental investigation of the effect of blade solidity on micro-scale and low tip-speed ratio wind turbines. *Exp. Therm. Fluid Sci.* **2023**, *140*, 110745. [CrossRef]
14. Birajdar, M.; Kale, S.; Sapali, S.N. Effects of design parameters on aerodynamic performance of new profile small wind turbine blades. In *ASME International Mechanical Engineering Congress and Exposition*; American Society of Mechanical Engineers: New York, NY, USA, 2015.
15. Sudarma, A.F.; Kholil, M.; Subekti, S.; Almahdy, I. The effect of blade number on small horizontal axis wind turbine (HAWT) performance: An experimental and numerical study. *Int. J. Environ. Sci. Dev.* **2020**, *11*, 555–560. [CrossRef]
16. Eltayesh, A.; Castellani, F.; Burlando, M.; Hanna, M.B.; Huzayyin, A.S.; El-Batsh, H.M.; Becchetti, M. Experimental and numerical investigation of the effect of blade number on the aerodynamic performance of a small-scale horizontal axis wind turbine. *Alex. Eng. J.* **2021**, *60*, 3931–3944. [CrossRef]
17. Zawadzki, K.; Śmiechowicz, W.; Stępień, M.; Baszczyńska, A.; Tarkowski, M. Influence of the solidity ratio on the small wind turbine aerodynamics. *E3S Web Conf.* **2021**, *242*, 03006. [CrossRef]
18. Chaudhary, M.K.; Prakash, S. Experimental investigations and aerodynamic shape optimization of small horizontal axis wind turbine blades. *Trans. Can. Soc. Mech. Eng.* **2021**, *45*, 594–603. [CrossRef]
19. Porto, H.A.; Fortulan, C.; Porto, A.J.V. Wind tunnel measurements of a multibladed horizontal-axis small wind turbine. *J. Aerosp. Technol. Manag.* **2021**, *13*, e3921. [CrossRef]
20. Chaudhary, M.K.; Roy, A. Design & optimization of a small wind turbine blade for operation at low wind speed. *World J. Eng.* **2015**, *12*, 83–94. [CrossRef]
21. Vashkevitch, K.; Samsonov, V. New results of the study in wind turbine aerodynamics. *J. Wind Eng. Ind. Aerodyn.* **1992**, *39*, 173–177. [CrossRef]
22. Mayer, C.; Bechly, M.E.; Hampsey, M.; Wood, D.H. The starting behaviour of a small horizontal-axis wind turbine. *Renew. Energy* **2001**, *22*, 411–417. [CrossRef]
23. Kriswanto, M.; Setiawan, A.B.; Al-Janan, D.H.; Naryanto, R.F.; Roziqin, A.; Firmansyah, H.N.; Setiadi, R.; Darsono, F.B.; Jamari, A.S. Power Optimization of The Horizontal Axis Wind Turbine Capacity of 1 MW on Various Parameters of the Airfoil, an Angle of Attack, and a Pitch Angle. *J. Adv. Res. Fluid Mech. Therm. Sci.* **2023**, *103*, 141–156. [CrossRef]
24. Kaya, M.N.; Uzol, O.; Ingham, D.; Köse, F.; Buyukzeren, R. The aerodynamic effects of blade pitch angle on small horizontal axis wind turbines. *Int. J. Numer. Methods Heat Fluid Flow* **2023**, *33*, 120–134. [CrossRef]
25. Rahmatian, M.A.; Shahrbabaki, A.N.; Moeini, S.P. Single-objective optimization design of convergent-divergent ducts of ducted wind turbine using RSM and GA, to increase power coefficient of a small-scale horizontal axis wind turbine. *Energy* **2023**, *269*, 126822. [CrossRef]
26. Rahmatian, M.A.; Tari, P.H.; Mojaddam, M.; Majidi, S. Numerical and experimental study of the ducted diffuser effect on improving the aerodynamic performance of a micro horizontal axis wind turbine. *Energy* **2022**, *245*, 123267. [CrossRef]
27. Wang, S.H.; Chen, S.H. Blade number effect for a ducted wind turbine. *J. Mech. Sci. Technol.* **2008**, *22*, 1984–1992. [CrossRef]
28. Asl, H.A.; Monfared, R.K.; Rad, M. Experimental investigation of blade number and design effects for a ducted wind turbine. Renew. *Energy* **2017**, *105*, 334–343. [CrossRef]
29. Chen, T.Y.; Liao, Y.T.; Cheng, C.C. Development of small wind turbines for moving vehicles: Effects of flanged diffusers on rotor performance. *Exp. Therm. Fluid Sci.* **2012**, *42*, 136–142. [CrossRef]
30. Chen, T.Y.; Hung, C.W.; Liao, Y.T. Experimental study on aerodynamics of micro-wind turbines with large-tip non-twisted blades. *J. Mech.* **2013**, *29*, N15–N20. [CrossRef]
31. Wu, S.-J.; Ouyang, K.; Shiah, S.-W. Robust design of microbubble drag reduction in a channel flow using the Taguchi method. *Ocean Eng.* **2008**, *35*, 856–863. [CrossRef]
32. Ouyang, K.; Chen, T.Y.; Wu, J.Y. Numerical study of optimum parameter design for film cooling effectiveness by Taguchi method. *Int. J. Heat Fluid Flow* **2023**, *100*, 109118. [CrossRef]
33. Roy, R.K. *A Primer on the Taguchi Method*; Society of Manufacturing Engineers: Southfield, MI, USA, 2010.
34. Ross, P.J. *Taguchi Techniques for Quality Engineering*; McGraw-Hill: New York, NY, USA, 1996.
35. Chen, W.-H.; Wang, J.-S.; Chang, M.-H.; Mutuku, J.K.; Hoang, A.T. Efficiency improvement of a vertical-axis wind turbine using a deflector optimized by Taguchi approach with modified additive method. *Energy Convers. Manag.* **2021**, *245*, 114609. [CrossRef]
36. Chen, W.-H.; Wang, J.-S.; Chang, M.-H.; Hoang, A.T.; Lam, S.S.; Kwon, E.E.; Ashokkumar, V. Optimization of a vertical axis wind turbine with a deflector under unsteady wind conditions via Taguchi and neural network applications. *Energy Convers. Manag.* **2022**, *254*, 115209. [CrossRef]
37. Aksenov, A.; Dyadkin, A.; Luniewski, T.; Pokhilko, V. Fluid Structure Interaction Analysis Using Abaqus and FlowVision. In Proc. Abaqus User Conference. 2004. Available online: https://flowvision.ru/images/articles/2015/Fluid_Structure_Intera.pdf (accessed on 4 April 2024).

38. CAPVIDIA. *FlowVision 3.12.04 User Guide*; Chapter 6; CAPVIDIA: Houston, TX, USA, 2021.
39. Versteeg, H.K.; Malalasekera, W. *An Introduction to Computational Fluid Dynamics: The Finite Volume Method*; Pearson Education: London, UK, 2007.
40. Ouyang, K.; Wu, H.-W.; Huang, S.-C.; Wu, S.-J. Optimum parameter design for performance of methanol steam reformer combining Taguchi method with artificial neural network and genetic algorithm. *Energy* **2017**, *138*, 446–458. [CrossRef]